



**HAL**  
open science

## Evaluation of scanning transmission X-ray microscopy at the Mn L<sub>2,3</sub>-edges as a potential probe for manganese redox state in natural silicates

Franck Bourdelle, Emily Lloret, Cyril Durand, Laura Airaghi

### ► To cite this version:

Franck Bourdelle, Emily Lloret, Cyril Durand, Laura Airaghi. Evaluation of scanning transmission X-ray microscopy at the Mn L<sub>2,3</sub>-edges as a potential probe for manganese redox state in natural silicates. *Physics and Chemistry of Minerals*, 2021, 48 (4), 10.1007/s00269-021-01142-w . insu-03192509

**HAL Id: insu-03192509**

**<https://insu.hal.science/insu-03192509v1>**

Submitted on 8 Apr 2021

**HAL** is a multi-disciplinary open access archive for the deposit and dissemination of scientific research documents, whether they are published or not. The documents may come from teaching and research institutions in France or abroad, or from public or private research centers.

L'archive ouverte pluridisciplinaire **HAL**, est destinée au dépôt et à la diffusion de documents scientifiques de niveau recherche, publiés ou non, émanant des établissements d'enseignement et de recherche français ou étrangers, des laboratoires publics ou privés.

1 Title: **Evaluation of scanning transmission X-ray microscopy at the Mn L<sub>2,3</sub>-edges as a**  
2 **potential probe for manganese redox state in natural silicates**

3  
4 Authors: Franck Bourdelle<sup>a,\*</sup>, Emily Lloret<sup>a</sup>, Cyril Durand<sup>a</sup>, Laura Airaghi<sup>b</sup>

5  
6 Affiliations:

7 <sup>a</sup> Univ. Lille, Institut Mines-Télécom, Univ. Artois, Junia, ULR 4515 - LGCgE, Laboratoire  
8 de Génie Civil et géo-Environnement, F-59000 Lille, France

9 <sup>b</sup> University of Orléans, CNRS, BRGM, ISTO, UMR 7327, F-45071, Orléans, France

10

11 \*Corresponding authors:

12 Dr. Franck Bourdelle

13 Present mailing address: Laboratoire Génie Civil et géo-Environnement (LGCgE) –

14 Département des Sciences de la Terre, Université de Lille, Cité Scientifique, Bâtiment SN5,  
15 59655 Villeneuve d'Ascq Cedex, France.

16 E-mail address: franck.bourdelle@univ-lille.fr

17 Phone number: + 33 (0)3 20 43 41 13

18

19 ORCID:

20 Franck Bourdelle: 0000-0002-7136-8692

21 Emily Lloret: 0000-0003-0952-9202

22 Cyril Durand: 0000-0001-8341-8450

23 Laura Airaghi: 0000-0001-7032-2732

24

25

26

27

28 **Abstract**

29 Determining the Mn valence variation at the nanometer scale will be an important advance in  
30 the study of heterogeneous natural silicates. Here, the potential of the scanning transmission  
31 X-ray microscopy at the Mn L<sub>2,3</sub>-edges (640 - 655 eV) as a probe for manganese redox state is  
32 evaluated. For this purpose, several natural Mn-silicates (rhodonite, ardennite, piemontite,  
33 Mn<sup>4+</sup>-silicate, jacobsonite), covering several Mn valence, were analysed to identify the spectral  
34 parameters most sensitive to the Mn valence, regardless of the coordination environment, the  
35 crystal field strength, the nature and the length of the metal–ligand bonds, and the intra-  
36 atomic Coulomb and spin–orbit interactions. Two suitable spectral empirical calibrations are  
37 thus proposed, linking the Mn valence to two peak intensity ratios: one ratio of intensities  
38 from two energy points of the L<sub>2</sub> peak (at 651.7 and 655.2 eV), and one ratio of intensities  
39 from one energy point of the L<sub>2</sub> peak (at 655.2 eV) and one of the L<sub>3</sub> peak (at 641.6 eV).  
40 Thank to them, the first quantitative Mn valence maps are constructed, with a high spatial  
41 resolution (< 40 nm pixel size), opening the way to exhaustive crystallochemical studies of  
42 silicates containing Mn with different valences.

43

44 Key words: manganese valence; STXM; XANES spectroscopy; L<sub>2,3</sub>-edges; redox mapping;  
45 silicates

46

47 **Declarations**

48 Funding: This study was financially supported by LGCgE (laboratory funds).

49 Conflicts of interest/Competing interests: Not applicable.

50 Availability of data and material: XANES spectra are available on request from

51 [franck.bourdelle@univ-lille.fr](mailto:franck.bourdelle@univ-lille.fr)

52 Code availability: Not applicable.

53 Authors' contributions (optional): -

## 54 **1. Introduction**

55           Constraining redox conditions during sediment deposition, rock formation or  
56 mineralogical transformation is of primary importance to understand the P-T-X history  
57 (pressure-temperature-composition) of geological systems. Redox conditions are usually  
58 assessed by the analysis of minerals since they partly influence their chemical composition.  
59 The evaluation of redox conditions is often based on the iron redox state, i.e. by the  
60 quantification of the  $\text{Fe}^{3+}/\text{Fe}^{2+}$  ratio in minerals – mainly silicates, major constituents of crusts  
61 – when they can contain both divalent and trivalent cations (i.e. Inoue et al. 2018). More  
62 rarely, the redox state of other metals is investigated, as manganese. However, Mn – which  
63 can be present as  $\text{Mn}^{2+}$ ,  $\text{Mn}^{3+}$  and sometimes-but-rarely  $\text{Mn}^{4+}$  – could be a good indicator of  
64 paleo-conditions of rock formation (Loomer et al. 2007), even if Mn-silicates, specially P-T-  
65 X sensitive silicate solid solution such as phyllosilicates, are infrequent, at the very least not  
66 ubiquitous in sedimentary and metamorphic rocks, and that the Mn content of these silicates  
67 is low. In this way, Sussenberger et al. (2018) suggest that Mn content in chlorite could be a  
68 proxy for chemo-stratigraphic conditions in depositional environment. For their part, Bobos et  
69 al. (2018) establish a link between Mn-chlorite and Wolframite, the Mn content in chlorite  
70 becoming an indicator of W-Mo mineralisation.

71           Unfortunately, authors could not determine the  $\text{Mn}^{3+}/\text{Mn}^{2+}$  ratio which would have  
72 noticeably modified the chlorite structural formula calculation, and potentially the subsequent  
73 interpretations. In the past, different techniques have been envisaged for this purpose,  
74 including electron microprobe analysis (EMPA, e.g. Albee and Chodos 1970), X-ray  
75 photoelectron spectroscopy (XPS, e.g., Ilton et al. 2016) or X-ray absorption near edge  
76 structure (XANES) spectroscopy at the K-edge (e.g. Manceau and Gallup 2005; Manceau et  
77 al. 2012). However, none of these methods provides a nanometer-scale spatial resolution,  
78 which could be particularly useful to identify chemical and redox zonation patterns in low-  
79 temperature crystals (e.g. Bourdelle et al. 2018). On the other hand, several studies (e.g.,  
80 Garvie and Craven 1994; van Aken and Liebscher 2002) have shown that electron energy-loss

81 spectroscopy (EELS) carried out in a transmission electron microscope (TEM) is a powerful  
82 method for determining the redox state of transition metals at a submicrometric resolution,  
83 including Mn in silicates, but sometimes induces severe beam damage effects, such as  
84 electron beam-induced reduction of manganese (Lauterbach et al. 2000; de Groot et al. 2010;  
85 Livi et al. 2012). The XANES spectroscopy at the  $L_{2,3}$ -edges is often proposed as a powerful  
86 alternative and is increasingly used in the Earth sciences. Firstly, the X-ray energies required  
87 for XANES analysis are lower at the  $L_{2,3}$ -edges (between ~640 and 655 eV) than at the K-  
88 edge (between ~6500 and 6580 eV), allowing higher resolutions, i.e. < 0.1 eV and ~30 nm at  
89 existing synchrotron facilities. Secondly, the X-ray incident beam is less destructive for  
90 samples than the TEM-EELS electron beam.

91         The XANES spectroscopy at the  $L_{2,3}$ -edges is based on the  $2p \rightarrow 3d$  electronic  
92 transition, which is sensitive to – among other parameters – the metal valence (e.g. Garvie and  
93 Craven 1994). De Groot et al. (1994) describing in detail the complex physical basis of Mn  
94  $L_{2,3}$ -edges, underlined that Mn valence can be obtained from  $L_{2,3}$ -edge spectra by a multiplet  
95 calculation. However, this approach remains difficult to use in the case of natural minerals  
96 whose structure has not been beforehand determined. Otherwise, the Mn valence can be  
97 evaluated by fitting  $L_{2,3}$ -edge spectra with a combination of reference spectra, but this  
98 requires  $Mn^{2+}$ ,  $Mn^{3+}$ ,  $Mn^{4+}$  reference compounds, with Mn in the same local coordination  
99 environment than the studied sample. Consequently, several authors have turned to empirical  
100 approaches, trying to find a spectral parameter depending only (or at least, mainly) on the Mn  
101 valence. The white-line ratio, calibrated by van Aken and Liebscher (2002), is probably the  
102 best known, linking the formal transition metal valence to the ratio of integral intensity (over  
103 a 2 eV window) of the  $L_3$  and  $L_2$  excitation peaks. Recently, Wang et al. (2018) used the  
104 integrated L-edge intensity, considering it is proportional to the total number of  $3d$  holes  
105 localized in the X-ray absorber (normalized to this invariant edge jump), while Risch et al.  
106 (2017) proposed a linear correlation between Mn valence and the energy of the center of  
107 gravity of the Mn  $L_3$ -edge. But these methods, a review of which was proposed by Tan et al.

108 (2013), were often calibrated for Mn-oxides, but were not tested on Mn-silicates, which  
109 present specific structures.

110 Moreover, synchrotron facilities make possible to carry out Mn L<sub>2,3</sub>-edge XANES  
111 spectroscopy with a scanning transmission X-ray microscope (STXM), one spectrum being  
112 one image pixel of the studied sample area (e.g. Bourdelle et al. 2013). This makes it possible  
113 to consider extracting quantitative maps of Mn valence over the entire area of interest, very  
114 useful for heterogeneous natural samples containing mixed oxidation state Mn species. Pecher  
115 et al. (2003) explore the feasibility of such maps extracted from STXM-XANES data, in order  
116 to characterize the Mn charge state distribution in biominerals. Unfortunately, in absence of  
117 empirical calibration based on a spectral intensity ratio rather than an integrated area or a  
118 center of gravity calculation, the resulting maps remain qualitative.

119 From these observations, we want to evaluate the potential of the scanning  
120 transmission X-ray microscopy at the Mn L<sub>2,3</sub>-edges as a probe for manganese redox state  
121 investigations in natural silicates, defining a suitable spectral empirical calibration allowing to  
122 construct quantitative Mn valence maps with a high spatial resolution (nanoscale).

123

## 124 **2. Materials and methods**

### 125 2.1. Natural samples

126 Samples used in this study were natural silicates, containing various Mn amount and  
127 covering the three common Mn redox state (2+, 3+, 4+). As the shape of the Mn L<sub>2,3</sub>-edge  
128 spectra can be influenced by, among others parameters, the Mn coordination, one oxide  
129 presenting Mn in tetrahedral coordination sites is also considered. Particles transparent to soft  
130 X-rays are needed to measure XANES spectra in the transmission mode of STXM, therefore  
131 samples are prepared as grounded powders dispersing in ethanol; a drop of which is placed  
132 (then evaporated) on a carbon holey support film placed on a 200 mesh copper grid.

133 The selected silicates are rhodonite, ardenite, piemontite and a Mn<sup>4+</sup>-silicate (Table  
134 1), for which chemical composition has been verified by Energy-dispersive X-ray

135 spectroscopy, the EDX probe being coupled to a Scanning electron microscopy (QUANTA  
136 200 SEM instrument operating at 15 kV with a 1.5 nA current; mineral standards used for  
137 EDX probe calibration: albite, diopside, orthoclase, garnet and MnTiO<sub>3</sub>; ZAF correction  
138 applied). Rhodonite is a Mn<sup>2+</sup> pyroxenoid, where Mn is mainly in 6 coordination, sometimes  
139 in 7 (Smyth and Bish 1988; Nelson and Griffen 2005). Mn is therefore in distorted octahedral  
140 sites, defined by Mn-O bonds. The rhodonite sample used here, whose formula is  
141 Ca<sub>0.15</sub>Mn<sub>0.85</sub>SiO<sub>3</sub>, comes from Gambaseta (Liguria, Italia). Ardennite is a Mn<sup>2+</sup> sorosilicate  
142 described by the following formula: Mn<sub>4</sub>Al<sub>4</sub>(AlMg)(AsO<sub>4</sub>)(SiO<sub>4</sub>)<sub>2</sub>(Si<sub>3</sub>O<sub>10</sub>)(OH)<sub>6</sub>. In it, Mn is  
143 located in large polyhedron, based on 5 coordination via Mn-O bonds, and 2 additional  
144 coordination via Mn-OH bonds (Donnay and Allmann 1968). Here, one specimen of As-  
145 Ardennite from Salm-Château (Ardennes, Belgium) was studied; the composition does not  
146 present an excess of Mn (< 4 atoms per formula unit), all Mn is consequently assumed as  
147 Mn<sup>2+</sup> (Nagashima and Armbruster 2020). Piemontite is a Mn-rich epidote, where Mn is in  
148 trivalent form and occupies octahedral sites. The selected specimen comes from the Prabornaz  
149 mine (Aosta, Italia), with the verified chemical formula  
150 Ca<sub>2.05</sub>(Al<sub>1.68</sub>Fe<sup>3+</sup><sub>0.49</sub>Mn<sup>3+</sup><sub>0.83</sub>)(Si<sub>2.0</sub>O<sub>7</sub>)(Si<sub>1.0</sub>O<sub>4</sub>)O(OH). The last studied Mn-silicate, a rare type  
151 of silicates that contains tetravalent Mn similarly to stavelotite-(La), was sampled at  
152 Eveslogchorr (Murmansk Oblast, Russia) combined with pectolite and has the determined  
153 empirical formula: Na<sub>0.3</sub>Ca<sub>1.4</sub>Fe<sup>3+</sup><sub>0.3</sub>Mn<sup>4+</sup><sub>5</sub>SiO<sub>14</sub>. A jacobsite sample, from Langban, (Filipstad,  
154 Sweden), was also analysed. Jacobsite is an Mn<sup>2+</sup> oxide belonging to the spinel group, with  
155 the common formula MnFe<sub>2</sub>O<sub>4</sub>. As a “normal spinel”, Mn<sup>2+</sup> occupies tetrahedral sites formed  
156 by 4 oxygens (Bosi et al. 2019).

157

158 Table 1: Samples used for STXM-XANES Mn L<sub>2,3</sub>-edge investigations to Mn mean valence  
159 quantification

Type	Sample	Location	Mn valence	Position of major peaks (eV)	
				L <sub>3</sub>	L <sub>2</sub>
Silicate	Rhodonite	Gambaseta (Liguria, Italia)	2+	641.6	654.1



Silicate	Ardennite	Salm-Château (Ardennes, Belgium)	2+	641.6	654.1
Silicate	Piemontite	Prabornaz mine (Aosta, Italia)	3+	643.2	654.4
Silicate	Mn <sup>4+</sup> -silicate	Eveslogchorr (Murmansk Oblast, Russia)	4+	644.6	655.2
Oxide	Jacobsite	Langban (Filipstad, Sweden)	2+	641.6	654.1

160

## 161 2.2. STXM and XANES spectroscopy

162 The STXM is able to record the transmitted soft X-ray intensity on each point of the  
163 pluri-micrometric-sized area of interest for each defined energy. Therefore, STXM gives 2D  
164 images for which each pixel represents a soft X-ray absorption spectrum. This is of great  
165 interest for mapping metal oxidation state variation into small crystallites (e.g. Bourdelle et al.  
166 2013). In the present study, STXM analyses were acquired on the PolLux beamline at the  
167 Swiss Light Source (SLS, Villigen, Switzerland). The characteristics of the beamline are  
168 detailed by Raabe et al. (2008); the beam was in circular-polarisation configuration to avoid  
169 crystal lattice orientation dependency of analysis (see below). The scanning transmission X-  
170 ray microspectroscopy endstation allows to achieve stacks and linescans, i.e. a spectral map of  
171 an area and a sum of spectra for each pixel of a line, respectively. Stacks were recorded over  
172 the 635–660 eV energy range (Mn L<sub>2,3</sub>-edge) using a 0.2 eV spectral resolution and a 40 nm  
173 spatial resolution. Linescans were recorded over the same energy range, using a 0.1 eV  
174 spectral resolution. The dwell time per image- and energy- point was between 1 and 10 ms.  
175 Focus was checked systematically for each particle. STXM-XANES data were post-processed  
176 using the aXis2000 software (Hitchcock 2012). Beam damages caused by the incident beam  
177 were assessed by monitoring spectral changes at the Mn L<sub>2,3</sub>-edges with increasing dwell  
178 times up to 20 ms.

179

## 180 2.3. Spectrum processing

181 Spectra were extracted from stacks and linescans in form of optical density spectra  
182 (noted OD), obtained as  $OD = -\ln(I/I_0)$ , where I is the X-ray intensity transmitted from the  
183 sample, and I<sub>0</sub> is those recorded without samples. Then two steps of processing were applied  
184 on spectra:

- 185 (i) a linear background correction was applied to remove the contribution of lower energy  
186 absorption edges, so that the pre-edge region is set to 0 optical density.
- 187 (ii) the two edge steps resulting from transitions to unoccupied states in the continuum were  
188 subtracted using a double arctan function (Chen et al. 1995; van Aken and Liebscher  
189 2002; Broton et al. 2007) as:

190

$$191 \quad f(\Delta E) = \frac{h_1}{\pi} \left( \tan^{-1} \left[ \frac{\pi}{w_1} (\Delta E - E_1) \right] + \frac{\pi}{2} \right) + \frac{h_2}{\pi} \left( \tan^{-1} \left[ \frac{\pi}{w_2} (\Delta E - E_2) \right] + \frac{\pi}{2} \right) \quad (1)$$

192

193 where  $h_1$  and  $h_2$  are the step heights of the two arctan functions,  $w_1$  and  $w_2$  are fixed peak  
194 widths and  $E_1$  and  $E_2$  are the positions of the inflection points resulting in an energy near the  
195 edge onset. Broton et al. (2007) proposed setting the function slope  $w$  at 5 eV, to account for  
196 the slow onset of the continuum. Following this recommendation,  $w_1$  and  $w_2$  were fixed to 5  
197 eV. For each sample, four or five spectra on different particles were extracted to evaluate the  
198 spectral variability. A total of 23 spectra were thus used in this study.

199

### 200 **3. Results and discussion**

#### 201 3.1. Influences of Mn redox state, coordination and atomic environment on the shape of Mn 202 L<sub>2,3</sub>-edge XANES spectrum

203 X-ray absorption near edge structure spectra at the Mn L<sub>2,3</sub>-edges for Mn-silicates and  
204 jacobsite are shown in Figure 1, where peaks are identified by letters (from L<sub>3</sub>-a to L<sub>3</sub>-h and  
205 from L<sub>2</sub>-a to L<sub>2</sub>-e) and linear background is subtracted. These spectra result from transitions  
206 from 2*p* core electrons to 3*d* state, 4*s* state or continuum as follow:

- 207 - two strong absorption peaks, usually noted L<sub>3</sub> and L<sub>2</sub>, due to the spin-orbit splitting of  
208 2*p* level (van Aken and Liebscher 2002; Nishida et al. 2013) involving transitions  
209 from 2*p*<sub>3/2</sub> and 2*p*<sub>1/2</sub> states to empty 3*d* atomic orbitals, respectively. From a 2*p*<sup>6</sup>3*d*<sup>*n*</sup>  
210 ground state, the absorption process leads to a core-excited 2*p*<sup>5</sup>3*d*<sup>*n*+1</sup> final state, as 3*d*<sup>5</sup>  
211 for Mn<sup>2+</sup>, 3*d*<sup>4</sup> for Mn<sup>3+</sup> and 3*d*<sup>3</sup> for Mn<sup>4+</sup>, implying variations in absorption energy.

- 212 - edge jump steps at the bottom of  $L_3$  and  $L_2$  peaks, corresponding to  $2p \rightarrow$  continuum  
213 transitions.
- 214 - negligible contributions of  $2p \rightarrow 4s$  transitions, which are 20 times weaker in intensity  
215 than  $2p \rightarrow 3d$  transitions.

216 Each  $L_3$  and  $L_2$  peak consists of one major peak accompanied on both sides by several  
217 minor peaks. The energy position of these major peaks mainly depends (but not only) on the  
218 core-excited final state, i.e. Mn redox state: 641.6 and 654.1 eV for  $Mn^{2+}$  ( $L_{3-b}$  and  $L_{2-c}$ ,  
219 respectively; rhodonite, ardennite, jacobsonite), 643.2 and 654.4 eV for  $Mn^{3+}$  ( $L_{3-e}$  and  $L_{2-d}$ ,  
220 respectively; piemontite), 644.6 and 655.2 eV for  $Mn^{4+}$  ( $L_{3-f}$  and  $L_{2-e}$ , respectively;  $Mn^{4+}$ -  
221 silicate). In this way, spectra are qualitatively similar to those described in several previous  
222 studies, obtained using different analytical techniques (e.g. Garvie and Craven 1994; Morales  
223 et al. 2004; Zhang et al. 2010; Kubin et al. 2018).

224 Minor peaks arise from factors other than redox as their number, intensity and shape  
225 vary from one sample to another. Therefore,  $Mn^{2+}$  spectra present 3 minor peaks ( $L_{3-a}$ ,  $L_{3-d}$   
226 and  $L_{3-g}$  with a shoulder peak noted  $L_{3-h}$ ) around  $L_{3-b}$ , and 2 minor peaks ( $L_{2-a}$ ,  $L_{2-b}$ ) before  
227  $L_{2-c}$ , more intensive (related to the intensity of major peaks) for rhodonite than for ardennite.  
228  $Mn^{3+}$  and  $Mn^{4+}$  spectra have fewer minor peaks: only two, at the same (or very close) energy  
229 position than the  $L_3$  and  $L_2$   $Mn^{2+}$  major peaks, and one more at 642.3 eV ( $L_{3-c}$ ) only for  $Mn^{4+}$   
230 spectra. These minor peaks are also observed in previous studies (e.g. de Groot et al. 2010;  
231 Cuartero et al. 2016; Risch et al. 2017), especially on Mn-oxide spectra, and are influenced by  
232 the Mn valence and coordination environment, the crystal field strength, the nature and the  
233 length of the metal–ligand bonds, and the intra-atomic  $3d-3d$  and  $2p-3d$  Coulomb and spin–  
234 orbit interactions in the  $2p$  core and  $3d$  orbitals.

235 Here, no complex calculations or multiplet analyses were used to describe spectrum shape in  
236 detail as the aim of the present study is to propose an easy-to-use approach to empirically map  
237 the Mn valence in silicates. However, some comments can be made to explain (i) the general  
238 shape of the Mn-silicate spectra and (ii) the great similarity of them with Mn-oxide spectra.

239 In fact,  $3d$  orbitals consist of five  $d$  orbitals, as three have lobes between  $x$ ,  $y$ ,  $z$ -axis  
240 (noted  $d_{xy}$ ,  $d_{xz}$ ,  $d_{yz}$ ) and two have lobes on the axes (noted  $d_{z^2}$  and  $d_{x^2-y^2}$ ). In octahedral  
241 coordination site, the 6 ligands approach Mn along the axes, increasing by electrostatic  
242 repulsion the energy of  $d_{z^2}$  and  $d_{x^2-y^2}$  orbitals (called  $e_g$ ). Conversely,  $d_{xy}$ ,  $d_{xz}$ ,  $d_{yz}$  orbitals  
243 (called  $t_{2g}$ ) point between the ligands, that lowered their energies. This difference of energy  
244 between  $e_g$  and  $t_{2g}$  orbital groups defines the crystal field strength ( $\Delta_o$  or  $10Dq$ ) (Burns 1993).  
245 In the case of 6 coordinated  $Mn^{2+}$ , the  $t_{2g}$  spectral contribution is often assigned to the  $L_{3-a}$   
246 minor peak, while  $e_g$  is associated to the  $L_{3-b}$  major peak (Garvie and Craven 1994; de Groot  
247 et al. 1994),  $10Dq$  can be deducting from the energy distance between these two peaks. In the  
248 Figure 2, focused on the  $L_3$ -edge part of  $Mn^{2+}$  absorption spectra (edge jump steps were  
249 subtracted), the energy gap between  $L_{3-a}$  and  $L_{3-b}$  is very weak ( $< 1$  eV), suggesting a low  
250  $10Dq$  value. The comparison with  $10Dq$  calculations and estimates from experiments  
251 previously published (Garvie and Craven 1994; Garvie et al. 1994; Pérez-Dieste et al. 2004)  
252 confirms that  $10Dq$  value is probably around 0.5 or 1 eV. The energy difference between  $t_{2g}$   
253 and  $e_g$  orbital groups remains therefore weak enough for Mn to be in high-spin state (Burns  
254 1993), which is the most common spin configuration for Mn (Garvie and Craven 1994; de  
255 Groot 1994). The Figure 2 also shows that the energy position of  $L_{3-a}$  is always the same  
256 whatever the  $Mn^{2+}$  mineral studied in our conditions, but that its intensity (related to  $L_{3-b}$   
257 major peak intensity) is variable. This observation is also suitable for other minor peaks  $L_{3-d}$   
258 and  $L_{3-g}$ , suggesting the contribution of another significant factors. In fact,  $Mn^{2+}$  in rhodonite,  
259 ardenite and jacobsite is located in different coordination sites, with different Mn-ligand  
260 bond length and different type of ligands. In rhodonite,  $Mn^{2+}$  occupies octahedral sites slightly  
261 distorted, elongated, due to the global structure, linked to 6 O (Smyth and Bish 1988). This  
262 configuration leads to an energy splitting between  $d_{x^2-y^2}$  and  $d_{z^2}$  orbitals ( $E_{d_{x^2-y^2}} > E_{d_{z^2}}$ ) on the  
263 one hand, and between  $d_{xy}$  and  $d_{xz}$ ,  $d_{yz}$  orbitals ( $E_{d_{xy}} > E_{d_{xz}}$  and  $E_{d_{yz}}$ ) on the other hand. In  
264 ardenite,  $Mn^{2+}$  is located in large polyhedron with a 6 or 7 coordination configuration, with  
265 O and OH as ligands (Donnay and Allmann 1968), also implying a substantial change in

266 orbital energies. In jacobsite,  $Mn^{2+}$  is surrounded by 4 O in a tetrahedral site. But in this case,  
267 the 4 ligands are closer to the  $d_{xy}$ ,  $d_{xz}$ ,  $d_{yz}$  orbitals ( $t_2$ ) than to the  $d_{z^2}$ ,  $d_{x^2-y^2}$  orbitals (e),  
268 leading to an inversion of the splitting energy,  $t_2$  orbital group having higher energy than e  
269 orbital group (Burns 1993). Differences in spectrum shapes, especially the intensities of  $t_{2g}$  or  
270  $t_g - L_3$ -a (virtually disappeared in the case of jacobsite),  $L_3$ -d and  $L_3$ -g peaks, must be related  
271 to the coordination and the ligands of Mn. From an empirical point of view, the intensity of  
272 minor peaks decreases proportionally to the number of Mn-O bonds. On the other hand, the  
273 similarity of Mn-silicates (i.e.  $Mn^{2+}$ ,  $Mn^{3+}$  and  $Mn^{4+}$  -silicates) and Mn-oxides spectra (from  
274 this study and literature) tends to indicate that, as a first approximation, the extended atomic  
275 environment (i.e. beyond the coordination site receiving Mn) has negligible influence  
276 compared to that of the near coordination.

277         Consequently, an empirical calibration linking a spectral parameter to the Mn mean  
278 valence must be mainly based on major peaks, most sensitive to redox, without taking into  
279 account an energy window (as white line ratio method) that might include minor peaks, most  
280 sensitive to the Mn coordination and the surrounding atomic environment. An empirical  
281 calibration is possible especially since the  $10Dq$  is weak (van der Laan and Kirkman 1992).

282

### 283 3.2. Mn redox state estimation from $L_{2,3}$ -edge XANES spectra

284         As three valence states of Mn could be present in silicates, it is not possible to  
285 determine easily, directly and empirically the relative proportion of each of them. As an  
286 alternative, XANES spectra allow to assess the Mn mean valence which, coupled to a  
287 structural formula obtained with an independent method, gives a strong indication of the  
288 likely  $xMn^{2+} + yMn^{3+} + zMn^{4+}$  combination.

289         As referenced in the Figure 1, the main variation in the XANES spectra of silicates  
290 with the Mn valence involves the energy position of the  $L_3$  major peak. More precisely, the  $L_3$   
291 major peak shifts to higher energies with increasing Mn charge, by a step of 1.4-1.6 eV.  
292 However, because this step and Mn valence are not linearly linked, Risch et al. (2017) prefer

293 to use the center of gravity of the L<sub>3</sub>-edge. From Mn-oxides, authors propose a linear  
294 correlation implying to take in consideration the L<sub>3</sub> minor peaks in addition to major peaks. A  
295 such correlation was established here for silicates (Figure 3), and demonstrates the influence  
296 of minor peaks, i.e. of the type of coordination sites in which Mn occurs. Considering only the  
297 mineral phases where Mn occupies octahedral sites (piemontite, rhodonite) and Mn<sup>4+</sup>-silicate,  
298 the relationship between nominal Mn valence and the L<sub>3</sub> center of gravity is linear, with a R<sup>2</sup>  
299 = 1. However, taking into account the ardennite in which Mn occupies large polyhedron or  
300 jacobsite in which Mn is in tetrahedral sites, the energy position of the L<sub>3</sub> center of gravity for  
301 Mn<sup>2+</sup> phases depends on L<sub>3</sub>-a, L<sub>3</sub>-d and L<sub>3</sub>-g peak weight and not only of Mn redox state.  
302 Mainly, the L<sub>3</sub> center of gravity is a spectral parameter including a peak area, not extractable  
303 from a stack. This approach therefore does not allow to easily map the Mn valence from  
304 STXM-XANES data.

305 In order to construct a redox map, it becomes therefore necessary to propose a new  
306 purely-empirical calibration of Mn valence with a simple spectral parameter, using selected  
307 energy points (and not a spectral surface as white line ratio or center of gravity), that does not  
308 need to have any physical significance (as an intensity ratio). Considering only the silicates  
309 (jacobsite is excluded) and the 13 identified peaks (Figure 1), 78 ratios of two peak intensities  
310 can be calculated, plus their inverses, namely 156 possibilities. But only 12 peak intensity  
311 ratios are in correlation with the Mn valence with a coefficient of determination higher than  
312 0.98. In fact, the R<sup>2</sup> is very poor for intensity ratios implying major peaks of Mn<sup>3+</sup> and minor  
313 peaks of Mn<sup>2+</sup> (Figure 2). On the 12 peak intensity ratios correlated to Mn valence, 3 only  
314 used peaks from L<sub>3</sub> peak, 6 only used peaks from L<sub>2</sub> peak, and 3 used peaks from L<sub>3</sub> and L<sub>2</sub>  
315 peaks. Among them, we prefer those using peaks common to several valences and major  
316 peaks. Two correlations are therefore selected as calibration. The selected spectral parameter  
317 in the first calibration is a ratio between the intensities at two energy points of the L<sub>2</sub>-edge, i.e.  
318 at L<sub>2</sub>-a in Mn<sup>2+</sup> spectra (651.7 eV) and at the L<sub>2</sub>-e major peak in Mn<sup>4+</sup> spectra (655.2 eV). The  
319 spectral parameter is then expressed as follows:

320

$$321 \quad R_{L_2} = \frac{I(\text{at } 655.2 \text{ eV})}{I(\text{at } 651.7 \text{ eV})}$$

322

323 From this parameter, the first calibration equation is (Figure 4a):

324

$$325 \quad \text{Mn mean valence} = \frac{R_{L_2} + 6.705}{3.512} \quad (2)$$

326

327 It shows a coefficient of determination ( $R^2$ ) of 0.999. The same  $R_{L_2}$  value is obtained for  
328 ardenite and rhodonite (and jacobsite, not used for calibration), showing that  $R^2$  is not  
329 influenced by the Mn atomic environment but only by the Mn valence. This perfect  
330 correlation can be used to map Mn valence on unknown samples, since only two images (at  
331 fixed energy, i.e. 651.7 and 655.2 eV) are required.

332 The spectral parameter defined in the second calibration is the ratio between the  
333 intensity at  $L_3$ -edge energy point (i.e. 641.6 eV, the energy position of the  $L_3$ -b major peak of  
334  $Mn^{2+}$  spectra) and the intensity at  $L_2$ -edge energy point (i.e. 655.2 eV, the energy position of  
335 the  $L_2$ -e major peak of  $Mn^{4+}$  spectra). The calibration equation is expressed as follows (Figure  
336 4b):

337

$$338 \quad \text{Mn mean valence} = \frac{R_{L_{2,3}} + 0.669}{0.386} \quad (3)$$

339 with

$$340 \quad R_{L_{2,3}} = \frac{I(\text{at } 655.2 \text{ eV})}{I(\text{at } 641.6 \text{ eV})}$$

341

342 The coefficient of determination for this second calibration ( $R^2$ ) is 0.984, slightly lower than  
343 the one of the first calibration. The difference between  $R_{L_{2,3}}$  values for rhodonite and  
344 ardenite (and jacobsite) suggests a contribution of Mn atomic environment in addition to the  
345 Mn valence dependence. However, taking an intensity on the  $L_3$ -edge (which is more intense

346 than the  $L_2$ ) and one on the  $L_2$ -edge improves the signal to noise ratio. As for the first  
347 correlation proposed, the construction of a Mn valence map from STXM-XANES data is  
348 made possible by equation 3.

349

### 350 3.3. STXM-XANES coupling: Mn redox mapping

351 The scanning properties of the microscope allow to record a stack of 125 energy  
352 images over the 635-660 eV with a spectral resolution of 0.2 eV. Equations 2 and 3 permit the  
353 Mn mean valence to be estimated from the spectrum intensities at two energies. This gives the  
354 possibility to easily map the Mn valence from two energy images, and use one of the two  
355 calibrations proposed.

356 In fact, two other XANES images are required in addition to the two images used for  
357 mapping, in order to subtract the background at each pixel of the images. Therefore, only four  
358 energy images should be selected to calculate the  $R$  parameter. In the Figure 5, the calibration  
359 procedure that uses the equation 3 and the  $R_{L_2,3}$  parameter is drawn as example (piemontite  
360 sample). It is obtained by extracting one image at 641.6 eV, one at 655.2 eV, one in the pre-  
361 edge (to apply the “linear background correction” at each pixel of the 641.6 eV image), and  
362 one beyond the energy corresponding to the  $L_2$  peak (to remove the linear background and the  
363 second edge step of the arctan function at each pixel of the 655.2 eV image). The ratio of  
364 corrected 641.6 and 655.2 eV images can then be used to determine the  $R_{L_2,3}$  for each pixel  
365 and to obtain the map of Mn redox state. In this way, the linear background is represented by  
366 only one energy at one energy position, so this point should be fairly close to the first peak  
367 (638 eV in Figure 5). In the case of spectra with a strong background noise, it is possible to  
368 make an “image average” (giving an average value of the linear pre-peak background) by  
369 selecting about 10 images between 625 and 639 eV, by adding them and then by dividing the  
370 resulting “image sum” by 10 thanks to the aXis2000 software.

371 If the equation 2 is chosen for calibration, the images required to calculate the  $R_{L_2}$   
372 parameter need to be selected at 651.7 eV ( $L_2$ -a), at 655.6 eV ( $L_2$ -e), at the inflexion point



373 between the  $L_3$  peak and the  $L_2$  peak (to remove the background from the 651.7 eV), and one  
374 beyond the  $L_2$  peak (to remove the linear background and the second edge step of the arctan  
375 function for each pixel of the 655.2 eV image). By applying the same procedure as before, the  
376 Mn map can be reconstructed only from the  $L_2$ -edge data.

377         Resulting quantitative Mn redox maps are a useful tool to identify the Mn mean  
378 valence of unknown nanometric particles, but have some limitations. On a map built from  
379  $R_{L2,3}$  parameter for a no-pure piemontite sample constructed with equation 3 (Figure 6), the  
380 Mn-free crystallites appear in white (Figure 5G and Figure 6) while in areas where the particle  
381 is too thick and/or highly concentrated in Mn, valence is overestimated (Figure 6B). In the  
382 first case, the absence of Mn leads to calculate the ratio between two too weak absorption  
383 pixels (Figure 5E and F). In the second case, a too high X-ray absorption cause an absorption  
384 saturation of the  $L_3$  peak, which is more intense than the  $L_2$  peak. This phenomenon generates  
385 a nonlinear response of the absorption detection, artificially modifying the relative peak  
386 intensities, affecting the  $R_{L2,3}$  calculation and overestimating the Mn valence. Although more  
387 sensitive to the signal/noise ratio, the use of the  $R_{L2}$  parameter and equation 2 to map the Mn  
388 valence, based exclusively on the  $L_2$  peak, may provide a favourable way to circumvent  
389 absorption saturation issues encountered with the  $L_3$  peak (Figure 6C).

390         The spatial averaging effect of the X-ray beam over the pixel size (i.e., 40 nm) must  
391 also be taking into account. This effect fixes the limit of the minimum distance over which  
392 phase contacts or phase rims can be discriminated.

393         Surpassing these limitations easily identifiable, the STXM-based XANES quantitative  
394 map becomes a precise tool, giving an estimate of Mn valence with a high spatial resolution,  
395 as demonstrated by the map of piemontite in the Figure 6.

396

### 397 3.4. Assessment of saturation and beam damage effects

398         Although EELS is known to cause more damage than STXM on the structure of  
399 minerals (e.g. de Groot et al. 2010), the latter is nonetheless a method that damages particles

400 during analysis if precautions are not taken. Potentially, the repeated scan of particles at each  
401 energy point of a spectrum can altered the structure of the crystallites, and consequently the  
402 Mn mean valence estimate. A stack recorded on a 5x5  $\mu\text{m}$  area, obtained with a spatial  
403 resolution of 50 nm, a spectral resolution of 0.2 eV and a dwell time of 5 ms per energy- and  
404 image- point results in a total analysis time of 2.5 hours (dead time excluded) and of 0.875 s  
405 per image-point. To evaluate beam damages, spectral changes at the Mn  $L_{2,3}$ -edges were  
406 monitored with increasing dwell times, from 1 to 20 ms per energy- and image- point. The  
407 resulting XANES spectra do not show significant changes, while  $R_{L2}$  and  $R_{L2,3}$  parameters are  
408 only slightly affected, varying by less than 5%. Consequently, the effect of beam damages on  
409 the Mn valence estimate is negligible in the typical dwell time range used during routine  
410 analyses.

411 The saturation of spectrum can also alter assessment of  $R_{L2}$  and  $R_{L2,3}$  parameters (see  
412 section 3.3). This phenomenon occurs when particles are too thick or too rich in Mn (or a  
413 combination of both), leading to a distortion of the spectrum. Hanhan et al. (2009) for Ca and  
414 Bourdelle et al. (2013) for Fe proposed to evaluate the maximum intensity of the major peak  
415 not to be exceeded to avoid saturation effect. Applying a similar approach, the maximum Mn  
416  $L_3$  peak intensity, below which the  $L_3/L_2$  peak intensity ratio varies linearly and the spectrum  
417 is undistorted, was determined. For this, a stack was recorded on a powder of piemontite  
418 sample ( $\text{Mn}^{3+}$ ) with particles of various thicknesses. Figure 7 plots the intensity of the  $L_3$   
419 major peak according to the one of  $L_2$  major peak for each image-point. The intensities of  
420 these two peaks increase linearly until  $\sim 0.25$  OD. When the particle is thick enough for the  $L_3$   
421 major peak intensity to exceed 0.25 OD, the  $L_3/L_2$  intensity ratio no longer evolves linearly,  
422 i.e. the intensity of  $L_2$  major peak increases faster than that of  $L_3$  major peak, reflecting the  
423 spectra distortion for the considered image-points. This observation is also valid for  $\text{Mn}^{2+}$  and  
424  $\text{Mn}^{4+}$  spectra. Consequently, all the quantitative data in this study were therefore obtained  
425 from areas presenting a  $L_3$  major peak intensity lower than 0.25 OD. It should be noted that  
426 Mn is much more sensitive to saturation phenomena than Fe (saturation effects at  $> 1.5$  OD at

427 the Fe L<sub>2,3</sub>-edges; Bourdelle et al. 2013), i.e. saturation effects appear at relatively low Mn  
428 content (concentration or weak sample thickness). On an indicative basis, piemontite, which  
429 is a phase that is not very rich in Mn, presents saturated spectra for a crystallite thickness  
430 higher than ~150 nm, while Mn-rich jacobsonite shows saturation effects on spectrum when  
431 crystallite thickness is around 70 nm.

432 The crystal orientation compared with the direction of polarisation of the X-ray beam  
433 may also influence the spectrum shape. This process is called linear dichroism (Benzerara et  
434 al. 2011), and can be thwart using a circular polarized beam as here. The residual dichroism  
435 effect was evaluated by comparing spectra from different piemontite particles with various  
436 orientation. No change in spectrum shape was observed, and the impact of particle orientation  
437 on the Mn mean valence estimate remained undetectable.

438

## 439 **5. Conclusion**

440 In the present work, we explore the possibility to construct quantitative Mn redox  
441 maps for silicates using the STXM coupled with XANES spectroscopy at the Mn L<sub>2,3</sub>-edges.  
442 With fairly limited precautions, we demonstrate that this type of maps could be obtained from  
443 two easy-to-use empirical calibrations linking the Mn mean valence to a simple ratio of  
444 intensities from selected energy positions. We applied this approach on a mix of piemontite  
445 and no-Mn phase sample, demonstrating the potential of it to assess the Mn valence at the  
446 nanoscale through micrometric areas. Even if calibrations and map construction have yet to be  
447 tested on silicates containing Mn under several oxidation states, as Mn-phyllsilicates, these  
448 results pave the way for the study of nanochemical zonation in heterogeneous silicates.

449

## 450 **Acknowledgements**

451 We are most grateful to the PSI SLS synchrotron, especially Benjamin Watts (PolLux  
452 beamline) for technical advice. Thanks are extended to Philippe Recourt (LOG, Univ. Lille)  
453 for sample preparation and to Francis Coune for providing ardennite sample. The authors

454 wish also to thank the editor and the two anonymous reviewers for comments and suggestions  
455 that improved the paper. This study was financially supported by LGCgE.

456

## 457 **References**

458 Albee AL, Chodos AA (1970) Semiquantitative electron microscope determination of  
459  $Fe^{2+}/Fe^{3+}$  and  $Mn^{2+}/Mn^{3+}$  in oxides and silicates and its application to petrologic  
460 problems. *Am Mineral* 55:491-501.

461 Benzerara K, Menguy N, Obst M, Stolarski J, Mazur M, Tyliczak T, Brown GE Jr, Meibom  
462 A (2011) Study of the crystallographic architecture of corals at the nanoscale by scanning  
463 transmission X-ray microscopy and transmission electron microscopy. *Ultramicroscopy*  
464 111:1268–1275

465 Bobos I, Noronha F, Mateus A (2018) Fe-, Fe,Mn- and Fe,Mg-chlorite: a genetic linkage to  
466 W, (Cu, Mo) mineralization in the magmatic-hydrothermal system at Borralha, northern  
467 Portugal. *Mineral Mag* 82:S259-S279

468 Bosi F, Biagioni C, Pasero M (2019) Nomenclature and classification of the spinel  
469 supergroup. *Eur J Mineral* 31:183-192

470 Bourdelle F, Beyssac O, Parra T, Chopin C (2018) Nanoscale chemical zoning of chlorite and  
471 implications for low-temperature thermometry: Application to the Glarus Alps  
472 (Switzerland). *Lithos* 314:551-561

473 Bourdelle F, Benzerara K, Beyssac O, Cosmidis J, Neuville DR, Brown GE, Paineau E (2013)  
474 Quantification of the ferric/ferrous iron ratio in silicates by scanning transmission X-ray  
475 microscopy at the Fe L-2,L-3 edges. *Contrib Mineral Petrol* 166:423-434

476 Brotton SJ, Shapiro R, van der Laan G, Guo J, Glans PA, Ajello JM (2007) Valence state  
477 fossils in Proterozoic stromatolites by L-edge X-ray absorption spectroscopy. *J Geophys*  
478 *Res Biogeosci* 112:G3

479 Burns R (1993) Mineralogical Applications of Crystal Field Theory (Cambridge Topics in  
480 Mineral Physics and Chemistry). Cambridge: Cambridge University Press.  
481 doi:10.1017/CBO9780511524899

482 Chen CT, Idzerda YU, Lin HJ, Smith NV, Meigs G, Chaban E, Ho GH, Pellegrin E, Sette F  
483 (1995) Experimental confirmation of the X-ray magnetic circular-dichroism sum-rules for  
484 iron and cobalt. *Phys Rev Lett* 75:152–155

485 Cuartero V, Lafuerza S, Rovezzi M, Garcia J, Blasco J, Subias G, Jiménez E (2016) X-ray  
486 absorption and emission spectroscopy study of Mn and Co valence and spin states in  
487  $\text{TbMn}_{1-x}\text{Co}_x\text{O}_3$ . *Phys rev B* 94:155117

488 de Groot FMF, de Smit E, van Schooneveld MM, Aramburo LR, Weckhuysen BM (2010) In-  
489 situ scanning transmission X-ray microscopy of catalytic solids and related nanomaterials.  
490 *Chem Phys Chem* 11:951–962

491 de Groot FMF (1994) X-ray absorption and dichroism of transition metals and their  
492 compounds. *J Electron Spectros Relat Phenomena* 67:529-622

493 Donnay G, Allmann R (1968)  $\text{Si}_3\text{O}_{10}$  Groups in the Crystal Structure of Ardennite. *Acta*  
494 *Cryst B* 24:845

495 Garvie LAJ, Craven AJ (1994) High-resolution parallel electron energy-loss spectroscopy of  
496 Mn L<sub>2,3</sub>-edges in inorganic manganese compounds. *Phys Chem Miner* 21:191-206

497 Garvie LAJ, Craven AJ, Brydson R (1994) Use of electron-energy loss near-edge fine  
498 structure in the study of minerals. *Am Mineral* 79:411-425

499 Hanhan S, Smith AM, Obst M, Hitchcock AP (2009) Optimization of analysis of soft X-ray  
500 spectromicroscopy at the Ca 2p edge. *J Electron Spectros* 173:44–49

501 Hitchcock AP (2012) aXis 2000 analysis of X-ray images and spectra. McMaster University,  
502 Hamilton

503 Ilton ES, Post JE, Heaney PJ, Ling FT, Kerisit SN (2016) XPS determination of Mn oxidation  
504 states in Mn (hydr)oxides. *Appl Surf Sci* 366:475–485

505 Inoue A, Inoue S, Utada M (2018) Application of chlorite thermometry to estimation of  
506 formation temperature and redox conditions. *Clay Miner* 53:143–158

507 Kubin M, Guo M, Kroll T, Löchel H, Källman E, Baker ML, Mitzner R, Gul S, Kern J,  
508 Föhlisch A, Erko A, Bergmann U, Yachandra V, Yano J, Lundberg M, Wernet P (2018)  
509 Probing the oxidation state of transition metal complexes: a case study on how charge and  
510 spin densities determine Mn L-edge X-ray absorption energies. *Chem Sci* 9:6813

511 Lauterbach S, McCammon CA, van Aken P, Langenhorst F, Seifert F (2000) Mossbauer and  
512 ELNES spectroscopy of (Mg, Fe)(Si,Al)O<sub>3</sub> perovskite: a highly oxidised component of the  
513 lower mantle. *Contrib Mineral Petrol* 138:17–26

514 Livi KJT, Lafferty B, Zhu M, Zhang S, Gaillot A-C, Sparks DL (2012) Electron Energy-Loss  
515 Safe-Dose Limits for Manganese Valence Measurements in Environmentally Relevant  
516 Manganese Oxides. *Environ Sci Technol* 46:970–976

517 Loomer D, Al T, Weaver L, Cogswell S (2007) Manganese valence imaging in Mn minerals  
518 at the nanoscale using STEM-EELS. *Am Mineral* 92:72-79

519 Manceau A, Gallup DL (2005) Nanometer-sized divalent manganese-hydrous silicate  
520 domains in geothermal brine precipitates. *Am Mineral* 90:371-381

521 Manceau A, Marcus MA, Grangeon S (2012) Determination of Mn valence states in mixed-  
522 valent manganates by XANES spectroscopy. *Am Mineral* 97:816–827

523 Morales F, de Groot FMF, Glatzel P, Kleimenov E, Bluhm H, Hävecker M, Knop-Gericke A,  
524 Weckhuysen BM (2004) In Situ X-ray Absorption of Co/Mn/TiO<sub>2</sub> Catalysts for Fischer-  
525 Tropsch Synthesis. *J Phys Chem B* 108:16201-16207

526 Nagashima M, Armbruster T (2010) Ardennite, tiragalloite and medaite: structural control of  
527 (As<sup>5+</sup>, V<sup>5+</sup>, Si<sup>4+</sup>)O<sub>4</sub> tetrahedra in silicates. *Mineral Mag* 74:55–71

528 Nelson WR, Griffen DT (2005) Crystal chemistry of Zn-rich rhodonite ("fowlerite"). *Am*  
529 *Mineral* 90:969-983

530 Nishida S, Kobayashi S, Kumamoto A, Ikeno H, Mizoguchi T, Tanaka I, Ikuhara Y,  
531 Yamamoto T (2013) Effect of local coordination of Mn on Mn-L2,3 edge electron energy  
532 loss spectrum. *J Appl Phys* 114:054906

533 Pecher K, McCubbery D, Kneedler E, Rothe J, Bargar J, Meigs G, Cox L, Nealson K, Tonner  
534 B (2003) Quantitative charge state analysis of manganese biominerals in aqueous  
535 suspension using Scanning Transmission X-ray Microscopy (STXM). *Geochim*  
536 *Cosmochim Acta* 67:1089–1098

537 Pérez-Dieste V, Crain J N, Kirakosian A, McChesney J L, Arenholz E, Young A T, Denlinger  
538 J D, Ederer D L, Callcott T A, Lopez-Rivera S A, Himpsel FJ (2004) Unoccupied orbitals  
539 of 3d transition metals in ZnS. *Phys Rev B* 70:085205

540 Raabe J, Tzvetkov G, Flechsig U, Böge M, Jaggi A, Sarafimov B, Vernooij MGC,  
541 Huthwelker T, Ade H, Kilcoyne D, Tyliczszak T, Fink RH, Quitmann C (2008) PolLux: A  
542 new facility for soft X-ray spectromicroscopy at the Swiss Light Source. *Rev Sci Instrum*  
543 79

544 Risch M, Stoerzinger KA, Han B, Regier TZ, Peak D, Sayed SY, Wei C, Xu Z, Shao-Horn Y  
545 (2017) Redox Processes of Manganese Oxide in Catalyzing Oxygen Evolution and  
546 Reduction: An in Situ Soft X-ray Absorption Spectroscopy Study. *J Phys Chem C*  
547 121:17682–17692

548 Smyth JR, Bish D L (1988) Crystal Structures and Cation Sites of the Rock-Forming Minerals  
549 London and Boston (Unwin-Hyman Ltd.). *Mineral Mag* 52:733-734

550 Sussenberger A, Pospiech S, Schmidt ST (2018) [MnO vertical bar SiO<sub>2</sub>, Al<sub>2</sub>O<sub>3</sub>, FeO, MgO]  
551 balanced log-ratio in chlorites: a tool for chemo-stratigraphic mapping and proxy for the  
552 depositional environment. 16th International Clay Conference (ICC) Location: Granada.  
553 *Clay miner* 53:351-375

554 Tan H, Verbeeck J, Abakumov A, van Tendeloo G (2012) Oxidation state and chemical shift  
555 investigation in transition metal oxides by EELS. *Ultramicroscopy* 116:24–33

556 van Aken PA, Liebscher B (2002) Quantification of ferrous/ferric ratios in minerals: new  
557 evaluation schemes of Fe L-23 electron energy-loss near-edge spectra. *Phys Chem Miner*  
558 29:188–200

559 Van der Laan G, Kirkman IW (1992) The 2p absorption spectra of 3d transition metal  
560 compounds in tetrahedral and octahedral symmetry. *J Phys: Condens Matter* 4:4189-4204

561 Wang H, Friedrich S, Li L, Mao Z, Ge P, Balasubramanian M, Patil DS (2018) L-edge sum  
562 rule analysis on 3d transition metal sites: from d10 to d0 and towards application to  
563 extremely dilute metallo-enzymes. *Phys Chem Chem Phys* 20:8166–8176

564 Zhang S, Livi KJT, Gaillot A-C, Stone AT, Veblen DR (2010) Determination of manganese  
565 valence states in (Mn<sup>3+</sup>, Mn<sup>4+</sup>) minerals by electron energy-loss spectroscopy. *Am*  
566 *Mineral* 95:1741–1746

567

## 568 **Figure captions**

569

570 **Fig. 1** Representative XANES spectra at the Mn L<sub>2,3</sub>-edges for the Mn-silicates and jacobsonite. The  
571 spectra have been normalised to the major L<sub>3</sub> peak intensity, and some of the spectra have been shifted  
572 vertically for clarity (normalised intensity with arbitrary units). The vertical lines indicate major peaks  
573 (solid lines) and minor peaks (dashed lines). Each peak is indexed, redox states and core-excited final  
574 state configurations are mentioned

575

576 **Fig. 2** Focus on L<sub>3</sub>-edge for Mn<sup>2+</sup> phases (rhodonite, ardenite, jacobsonite). The spectra have been  
577 normalised to the major L<sub>3</sub> peak intensity. Coordination (number of O ligands and sites) is specified  
578 for each phases

579

580 **Fig. 3** L<sub>3</sub>-edge center of gravity from XANES spectra versus Mn valence for the selected silicates.  
581 Error bars represent the standard deviation calculated on the base of 4 or 5 spectra for each sample.  
582 Value for jacobsonite is given for information, but not taken into account for calibration calculation

583



584 **Fig. 4**  $L_{2,3}$ -edge intensity ratio from XANES spectra versus Mn valence for the selected silicates. (A)  
585  $R_{L2}$  ratio, using selected intensities at two energy points (i.e. 651.7 and 655.2 eV) of the  $L_2$ -edge. (B)  
586  $R_{L2,3}$  ratio, using selected intensities at one energy point (i.e. 641.6 eV) of the  $L_3$ -edge and one energy  
587 point (i.e. 655.2 eV) of the  $L_2$ -edge. Error bars represent the standard deviation calculated on the base  
588 of 4 or 5 spectra for each sample, i.e. 18 spectra in total. Values for jacobsite are given for  
589 information, but not taken into account for calibration calculation

590

591 **Fig. 5** Determination of the Mn valence from 4 selected energy images: one image in the pre-edge (to  
592 apply the “linear background correction” at each pixel of the image; image A), one at 641.6 eV ( $L_3$ -b  
593 major peak of  $Mn^{2+}$ ; image B), one at 655.2 eV ( $L_2$ -e major peak of  $Mn^{4+}$ ; image C) and one beyond  
594 the  $L_2$ -edge (to remove the edge step of the arctan function; image D). Finally, the ratio of the  
595 resulting 641.6 and 655.2 eV images (E and F) can be used to determine the  $R_{L2,3}$  parameter at each  
596 pixel of the image and obtain Mn redox mapping (G). All images are OD images, where piemontite  
597 and no Mn-silicate are the light-grey and dark phases on image E, respectively. White scale: 1  $\mu m$

598

599 **Fig. 6** Quantitative Mn redox nanomapping on particles from no-pure piemontite sample. A: optical  
600 density image at 641.6 eV, where the piemontite and no-Mn silicate particles are the light-grey and  
601 white phases, respectively. B: manganese redox mapping, calculated from the  $R_{L2,3}$  parameter coupled  
602 with the Eq. (3). C: manganese redox mapping, calculated from the  $R_{L2}$  parameter coupled with the Eq.  
603 (2). The spatial averaging effect of the X-ray beam over the pixel size (i.e., 40 nm) sets the limit of the  
604 minimum distance (turquoise rims, underlined by a yellow square). No-Mn silicates, identified by blue  
605 dashed polygon on the OD image, appear in white on the redox map B and in black for no Mn  
606 absorption on the redox map C and image E of the Fig. 5. Areas where the particle thickness is too  
607 high to obtain no-saturated images (see section 3.4.) – highlighted by a purple polygon on the OD  
608 image – lead to the overestimate of Mn valence (pink and red zones of the redox map B), up to the  
609 total saturation (appearing in white on the map). Areas presenting no-too-thick piemontite particles  
610 (i.e. the rest of the OD image) appear in blue on the Mn redox maps, testifying of trivalent manganese

611

612 **Fig. 7** Difference, pixel by pixel, of intensity detected between the L<sub>3</sub> major peak and the L<sub>2</sub> major  
613 peak images (in which a pre-edge image was subtracted) for a no-pure piemontite sample (4661  
614 pixels). The dashed line was calculated from a quadratic equation. Insets: representative spectra and  
615 optical density image (641.6 eV) for a no-pure piemontite sample

Figure 1

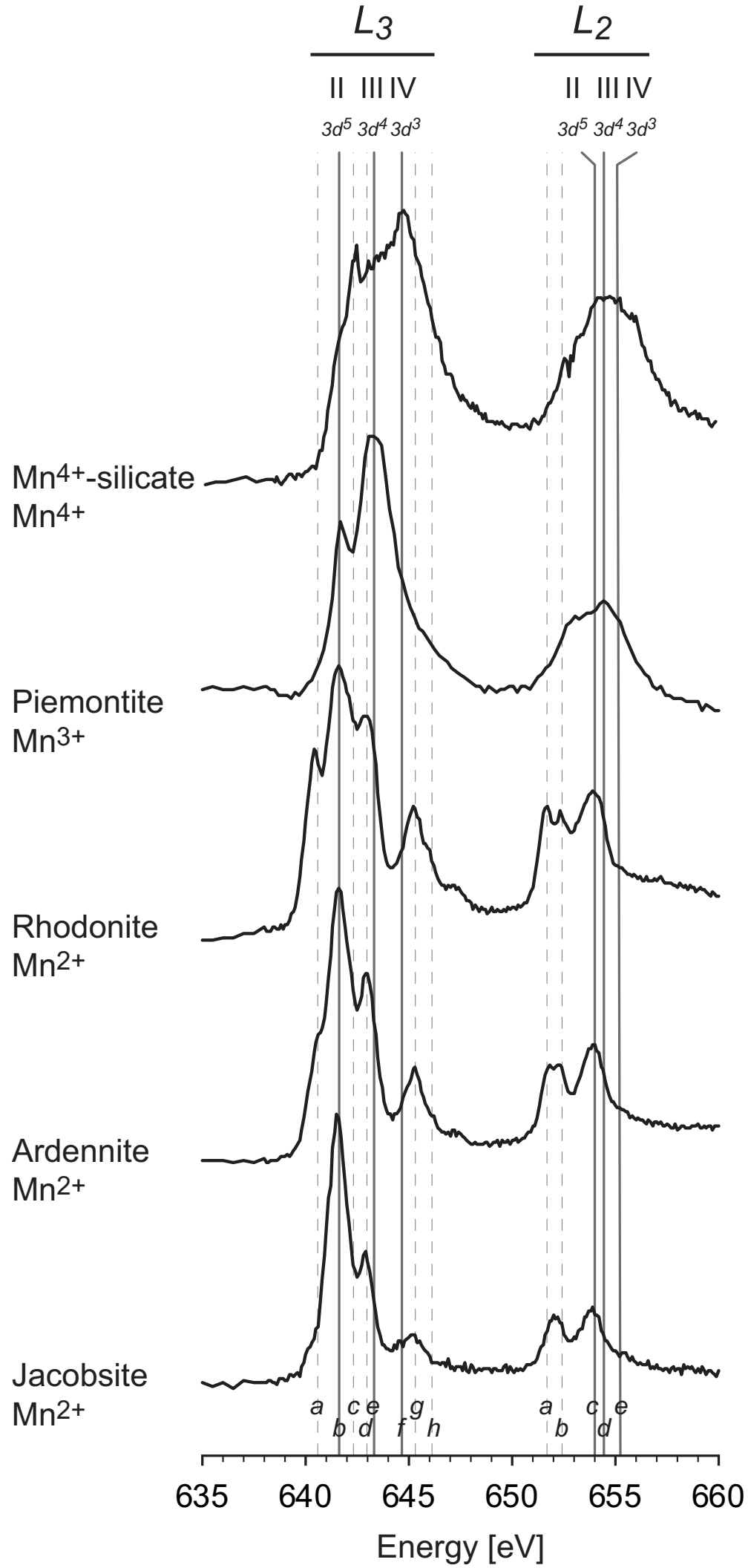


Figure 2

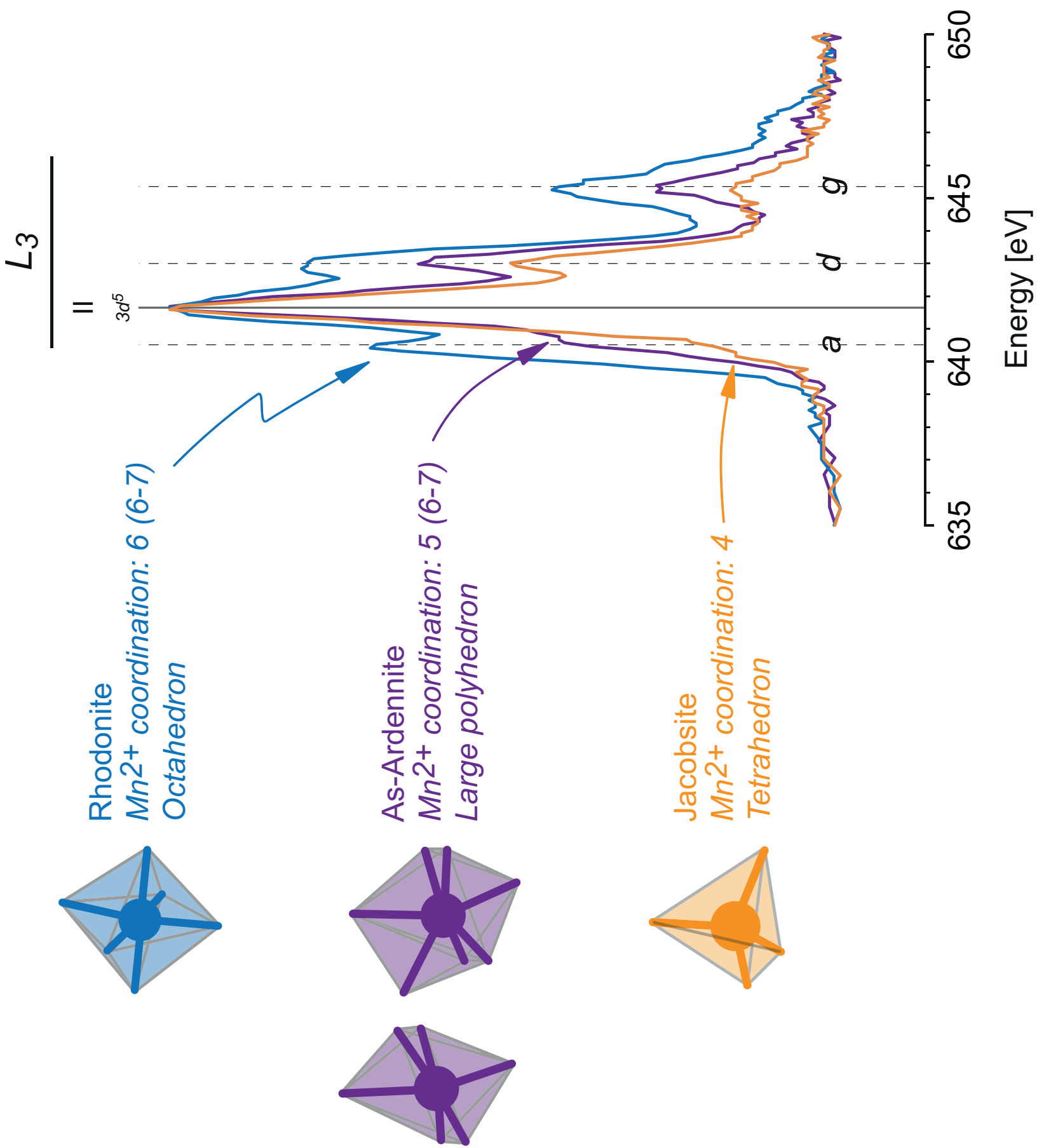


Figure3

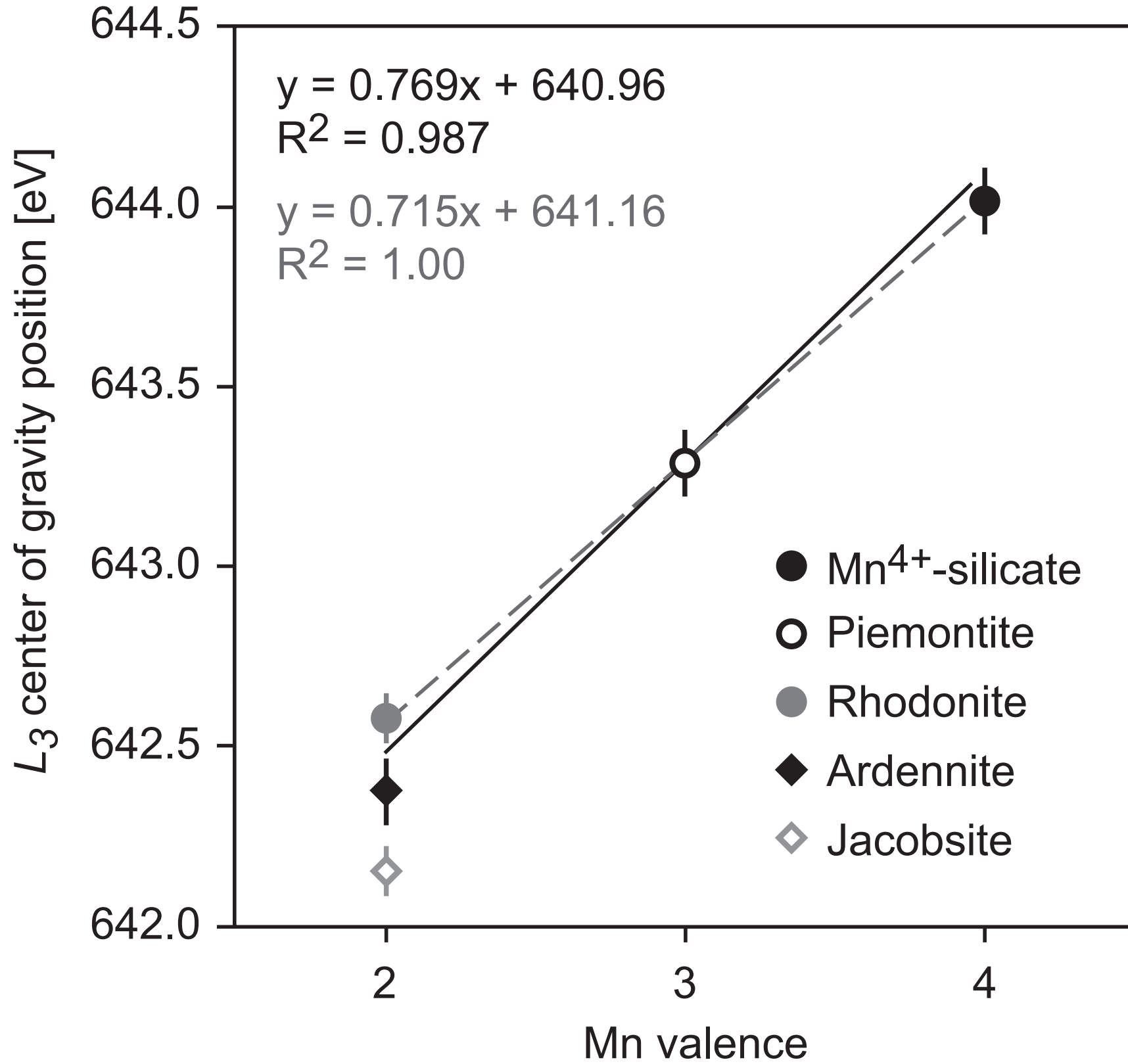
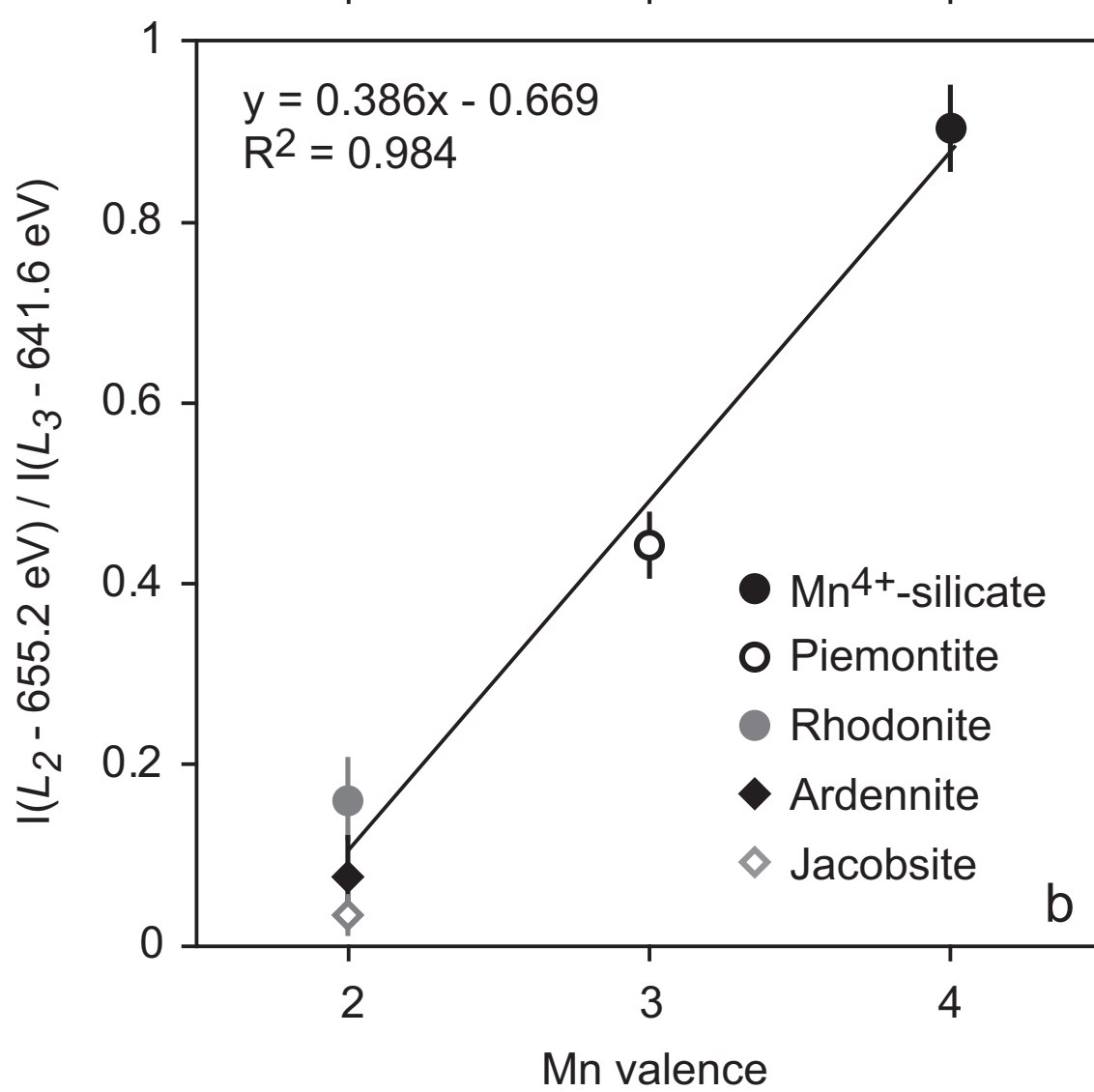
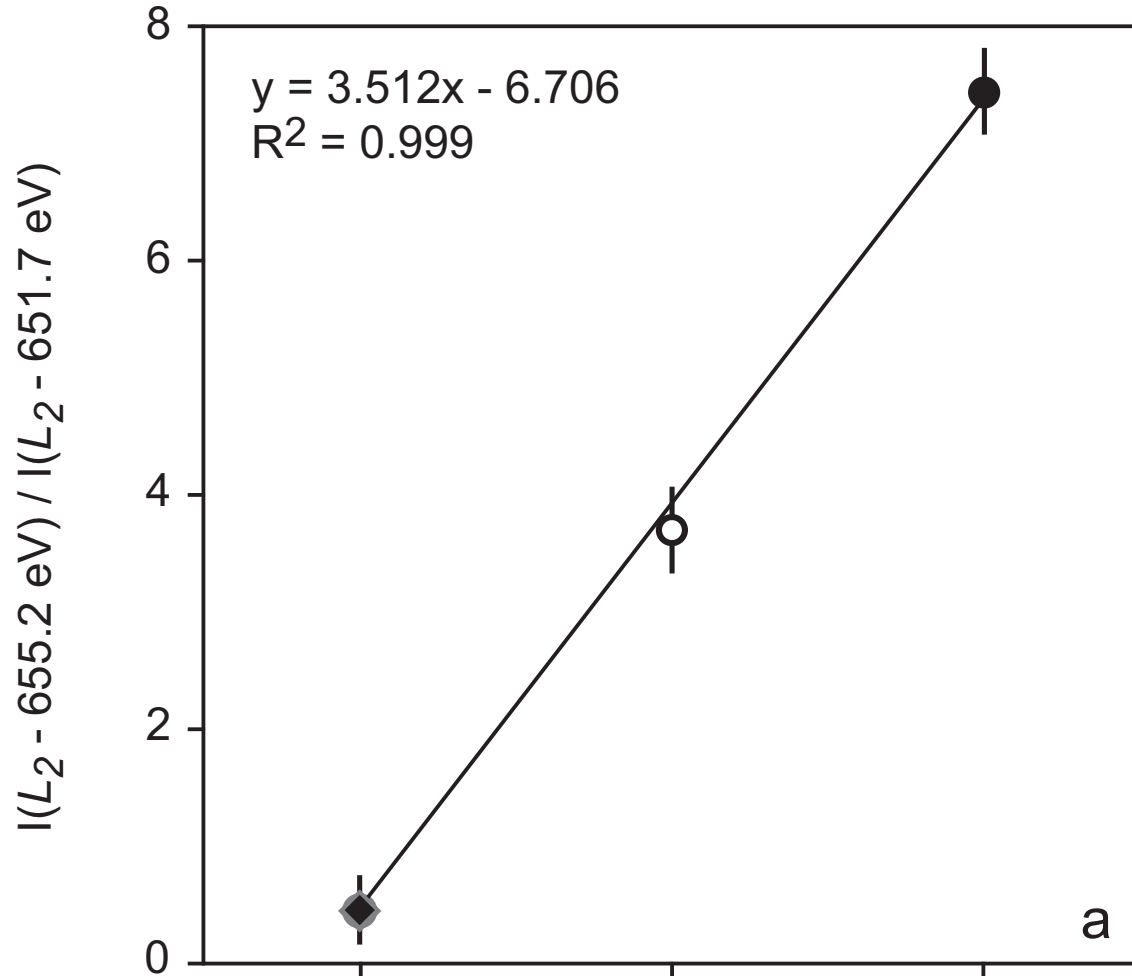
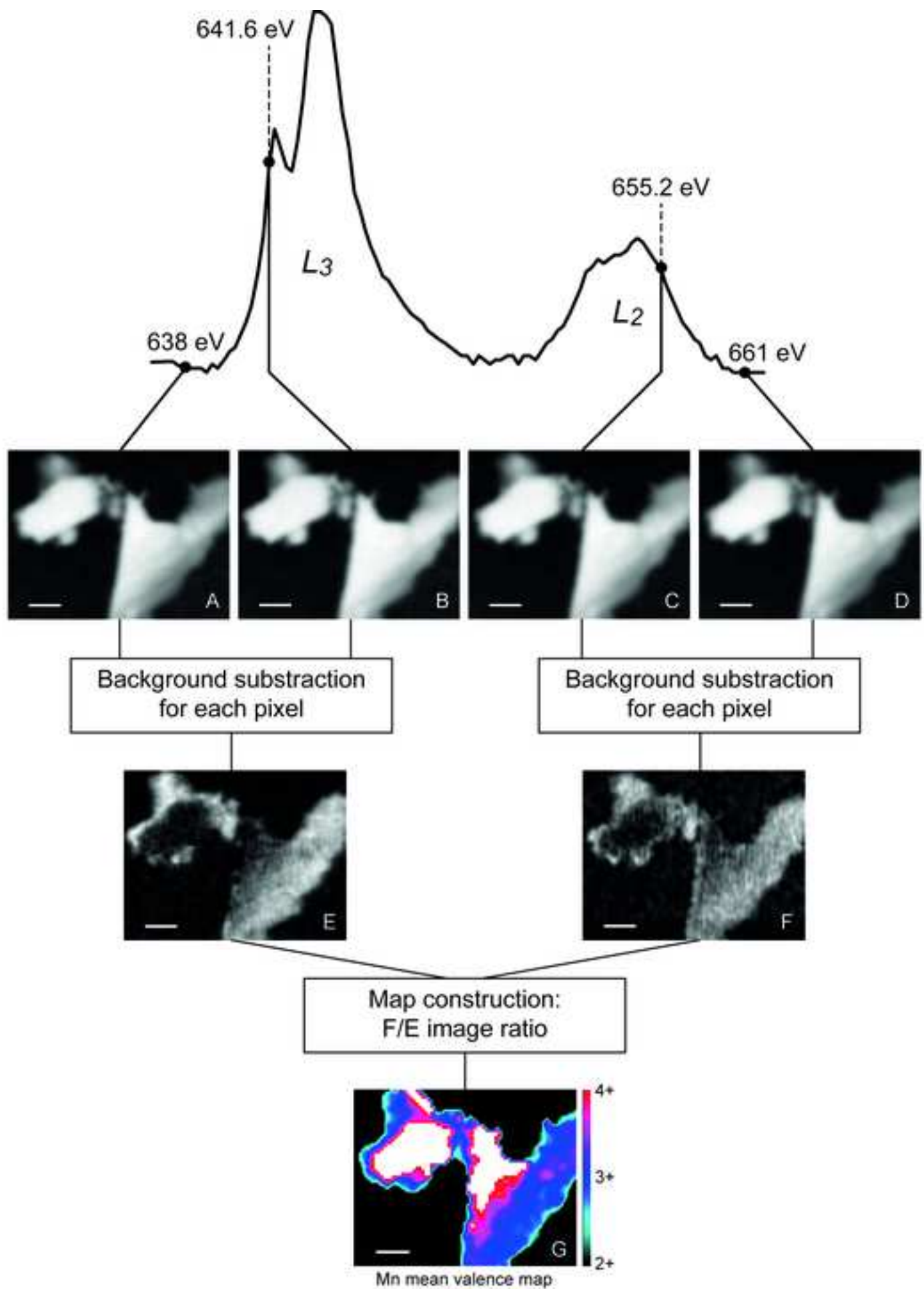


Figure 4





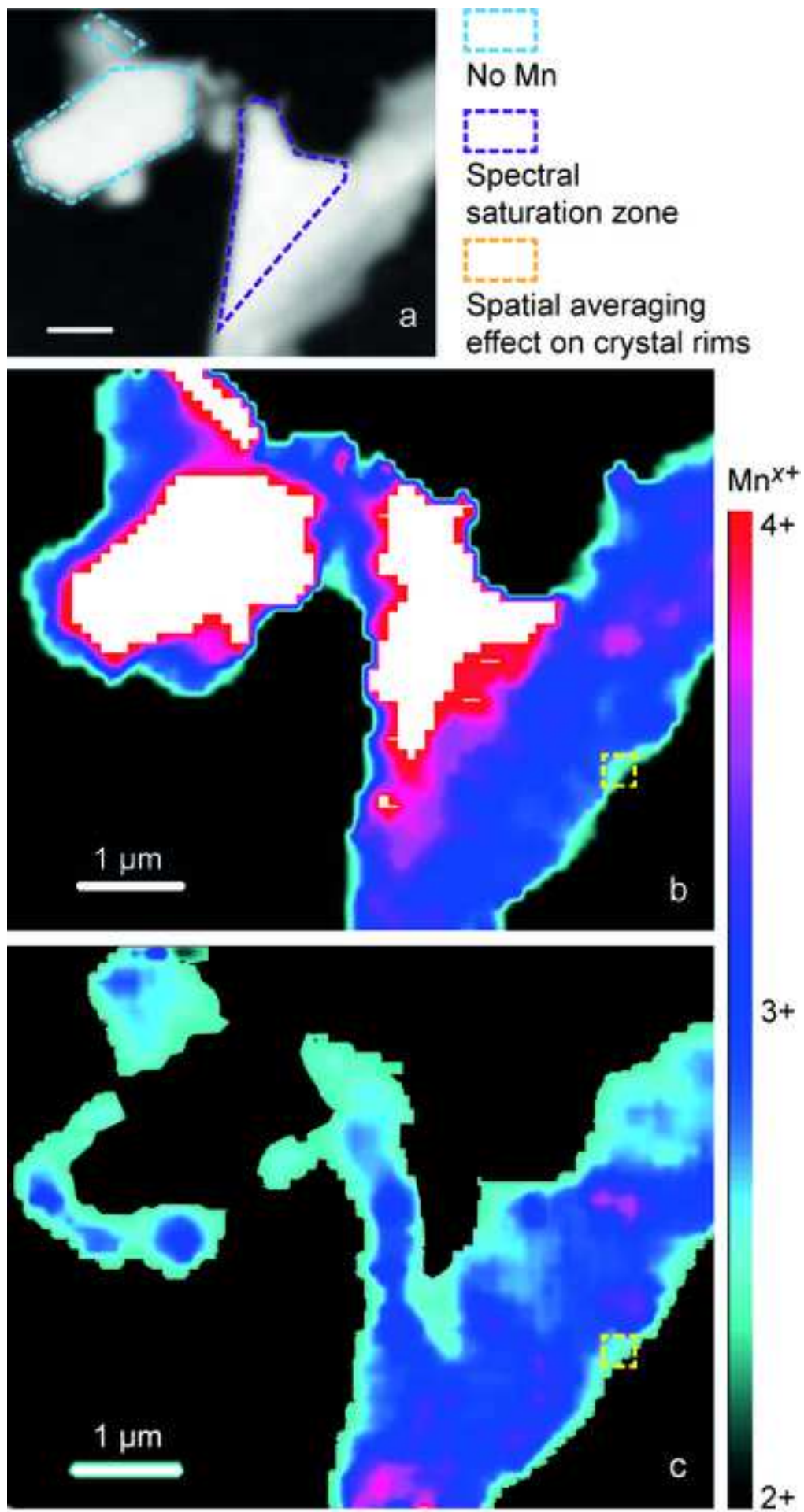




Figure 7

